Struct Multidisc Optim (2016) 53:1047–1067
DOI 10.1007/s00158-015-1377-y

RESEARCH PAPER

A level-set method for steady-state and transient natural convection problems

Peter Coffin[1] · **Kurt Maute**[1]

Received: 9 June 2015 / Revised: 8 September 2015 / Accepted: 30 September 2015 / Published online: 15 December 2015

Abstract This paper introduces a topology optimization method for 2D and 3D, steady-state and transient heat transfer problems that are dominated by natural convection in the fluid phase and diffusion in the solid phase. The geometry of the fluid-solid interface is described by an explicit level set method which allows for both shape and topological changes in the optimization process. The heat transfer in the fluid is modeled by an advection-diffusion equation. The fluid velocity is described by the incompressible Navier-Stokes equations augmented by a Boussinesq approximation of the buoyancy forces. The temperature field in the solid is predicted by a linear diffusion model. The governing equations in both the fluid and solid phases are discretized in space by a generalized formulation of the extended finite element method which preserves the crisp geometry definition of the level set method. The interface conditions at the fluid-solid boundary are enforced by Nitsche's method. The proposed method is studied for problems optimizing the geometry of cooling devices. The numerical results demonstrate the applicability of the proposed method for a wide spectrum of problems. As the flow may exhibit dynamic instabilities, transient phenomena need to be considered when optimizing the geometry. However, the computational burden increases significantly when the time evolution of the flow fields needs to be resolved.

✉ Peter Coffin
peter.coffin@colorado.edu

Kurt Maute
maute@colorado.edu

[1] Department of Aerospace Engineering Sciences, University of Colorado Boulder, Boulder, CO 80309, USA

Keywords Topology optimization · Level set methods · Heat transfer · Incompressible flow · Extended finite element method · Nitsche method

1 Introduction

Natural convection is the transport of heat via fluid motion driven by temperature dependent buoyancy forces. This mode of energy transport plays an important role in enclosed, sealed or vented systems, such as heat sinks and cooling devices in electronic systems. Heat transfer by natural convection is an attractive concept as it does not require additional mechanical devices, such as fans, and features robustness and simplicity (Baïri et al. 2014). As natural convection is dominated by the interplay of fluid motion and temperature evolution, the design of efficient heat transfer systems is challenging. Design decisions involve selecting a fluid with advantageous physical properties, placing heat sources, and determining the geometry of the enclosure and the internal structures, such as fins. This work presents a computational design optimization method for finding the geometry of thermal devices where the heat transport is dominated by natural convection.

The majority of work on optimizing natural convection systems has considered parametric geometry models with few design variables. For example, Morrison (1992) optimized the thickness and spacing of fins along with the thickness of a back-plane. Bahadur and Bar-Cohen (2005) treated the heat sink height and spacing of pin-fins as design variables. For such particular device geometries, the thermal performance can be approximated by either empirical relations or analytic models. To consider a larger design space and to allow for conceptual design changes in the optimization process, this work considers a topology optimization

approach and predicts the thermal response of the system by numerically solving a set of governing partial differential equations.

Topology methods typically describe the geometry of a body and the spatial arrangement of distinct materials within a body via the spatial distribution of a fictitious material. The volume fraction, or density, of the fictitious material is defined as a continuous function of the optimization variables, with the extrema representing distinct material phases. Density-based topology optimization methods, such as the SIMP (Solid Isotropic Material with Penalization) method, interpolate material properties as functions of the density to model geometry changes in the physics model. These methods have been successfully applied to a broad range of problems (Sigmund and Maute 2013; Deaton and Grandhi 2014). However, as the optimization process converges to material distributions with intermediate densities, the geometry cannot be clearly identified and the physical behavior is not correctly predicted. The latter issue affects in particular problems where boundary layer phenomena play an important role, such as flows at high Reynolds numbers and convective heat transport. To mitigate these shortcomings of density methods, Level Set Methods (LSMs) have been introduced to topology optimization. Phase boundaries are defined by the iso-contours of one or more level set functions (LSFs) and the material phase is defined by the signs of the LSFs. A recent review of LSMs in topology optimization is provided by van Dijk et al. (2013). This work considers a LSM for the design of natural convection problems.

To overcome the limitations of empirical and analytical models for convective heat transfer, engineers often describe the heat transfer in the solid by a linear diffusion model and approximate the heat flux at the fluid-solid interface by Newton's Law of Cooling (NLC) which assumes a constant, typically design-independent temperature in the fluid. This model has been used in topology optimization with density methods, for example, by Yin and Ananthasuresh (2002), Moon et al. (2004), Yoon and Kim (2005), Bruns (2007), Iga et al. (2009), Seo (2009) and Alexandersen (2011), and with LSMs by Yamada et al. (2011) and Coffin and Maute (2015). To further improve the prediction of the fluid temperature at the fluid-solid interface, the transport of heat in the fluid by convection and diffusion needs be considered. For low Mach number applications, where compressibility effects in the fluid can be neglected, the fluid temperature field is typically predicted by an advection-diffusion model where the fluid is assumed incompressible and described either by the Navier-Stokes or hydrodynamic Boltzmann equations. For forced convection problems, this class of models has been considered for topology optimization with the density method, for example, by Yoon (2010), Lee (2012), McConnell and Pingen (2012), Matsumori et al. (2013), Kontoleontos et al. (2013) and Koga et al. (2013). LSMs were studied for forced convection problems, for example, by Marck et al. (2013), Makhija and Maute (2015) and Yaji et al. (2015).

In contrast to forced convection problems, the work on topology optimization for natural convection problems is still in its infancy. Considering natural convection leads to a two-way coupled problem where fluid and thermal fields are interacting. Temperature dependent buoyancy forces drive the flow which in turn alters the temperature field. As the strength of the buoyancy forces and the flow velocities increase, this interaction causes dynamic instabilities in the flow. To date, Alexandersen et al. (2014) and Alexandersen (2015) presented the first and only studies of topology optimization for natural convection design problems. They adopted a density method and modeled the thermal response by an advection-diffusion equation at steady-state in two and three dimensions. The flow is described by the incompressible Navier-Stokes equations with the Boussinesq approximation of the buoyancy forces. The stick condition at fluid-solid interface is enforced via Brinkman penalization and the thermal conductivity is defined as a function of the density. Alexandersen et al. (2014) studied 2D problems and observed convergence issues in the flow analysis. This issue is likely due to the steady-state flow model being not able to capture transient flow phenomena. Furthermore, these authors found that intermediate densities may yield large flow velocities and convective fluxes which can be beneficial to the objective, making penalization of intermediate material difficult. Alexandersen (2015) expand this approach to 3D problems at steady-state.

The goal of this study is to mitigate the issues caused by intermediate densities and to expand the work of Alexandersen (2014) onto transient problems. Instead of a density method, this work adopts an LSM to provide a crisp representation of material boundaries. Traditionally the level set function is updated via the solution of the Hamilton-Jacobi equation; see, for example, Allaire et al. (2002), Wang et al. (2003), Allaire et al. (2004) and Burger and Osher (2005). Here, parameters of the discretized LSF are defined by explicit functions of optimization variables and the resulting optimization problem is solved by a nonlinear programming (NLP) method. This approach is often referred to as explicit LSM and has been studied, for example, by Wang and Wang (2006), Luo et al. (2007) and Pingen et al. (2010). Explicit LSMs allow solving problems with multiple constraints by standard NLP schemes.

To consider a broad range of natural convection problems, the flow and temperature fields are considered transient. As the appearance of unsteady phenomena depends on the geometry, which changes in the optimization process, assuming a steady-state response may not be valid throughout the optimization process. Even if the flow and

temperature fields of the initial and optimized design converge to a steady-state response, designs emerging in the optimization process may trigger unsteady phenomena, leading to convergence issues in the forward analysis. This work models natural convection problems with a transient diffusion model in the solid phase and a transient advection-diffusion model in the fluid phase in two and three dimensions. The flow is described by the transient incompressible Navier-Stokes equations augmented by buoyancy forces modeled by the Boussinesq approximation. To preserve the crispness of the level set geometry description in the coupled model, the governing equations are discretized in space by a generalized formulation of the extended finite element method (XFEM). For an introduction to the XFEM the reader is referred to Fries and Belytschko (2006) and Khoei (2015). The XFEM bypasses the need to introduce fictitious materials and allows enforcing the boundary conditions directly at the fluid-solid interface. The thermal and fluid fields are advanced in time by an implicit time stepping scheme. The unsteady system response is accounted for in the formulation of the optimization and the computation of the design sensitivities. We will study the main characteristics of this approach by numerical examples.

This work is proceeded by Coffin and Maute (2015) where a simplified convection model based on NLC was studied using the explicit LSM-XFEM. A key finding of Coffin and Maute (2015) is that the NLC approximation promotes unrealistically thin fluid channels, as the NLC model over predicts the convective flux. This finding motivates the present work where the temperature in the fluid is resolved. The same explicit LSM-XFEM scheme has been studied for a variety of physical models. Makhija and Maute (2014) study fundamental issues using the XFEM in level set topology optimization. Makhija and Maute (2015) study forced convection using a hydrodynamic Boltzmann transport model and Jenkins and Maute (2015) study fluid-structure interaction problems.

The remainder of this paper is organized as follows: In Section 2, the characteristics and the formulation of the optimization problems considered in this study are described. Section 3 presents two approaches for parameterizing and discretizing the LSF. In Section 4, the natural convection model is described, including the XFEM discretization, the time stepping scheme, and the associated adjoint sensitivity analysis. Numerical examples are studied in Section 5. The insight gained from these studies are presented in Section 6.

2 The optimization problem

Natural convection problems feature a rich set of physical phenomena which need to be accounted for in the formulation of the optimization problem. In this section, we first discuss approaches to characterize natural convection problems and then introduce the formulation of the optimization problem considered in this study.

2.1 Natural convection design problems

The class of design problems considered in this work assumes a solid body immersed in fluid. An external heat flux is applied to the solid body and the fluid is enclosed by walls which are either assumed adiabatic or at a prescribed temperature. This configuration idealizes a broad range of problems where natural convection plays an important role for heat transfer; see Section 1.

The energy transport in the solid phase is due to diffusion and in the fluid phase is due to both, diffusion and convection. Diffusion is the process of heat transfer between neighboring material and convection being the heat transfer due to the motion of material. The Rayleigh number is a non-dimensional parameter that characterizes the relative strength of convective to conductive heat transport in natural convection flows and is defined as:

$$Ra = \frac{|\mathbf{g}|\beta_F \Delta T L_c^3}{\nu_F \alpha_F}, \quad \alpha_F = \frac{\kappa_F}{\rho_F c_{p,F}} \tag{1}$$

where $|\mathbf{g}|$ is the magnitude of the gravitational acceleration vector, β_F the fluid thermal expansion coefficient, ΔT the temperature difference between the fluid-solid interface and the far-field fluid, L_c the characteristic length, and ν_F the fluid kinematic viscosity. The fluid diffusivity, α_F, is the ratio of the fluid heat conductivity, κ_F, and the product of fluid density, ρ_F, and specific heat capacity, $c_{p,F}$. Large Ra values describe configurations dominated by convective energy transport.

For forced convection problems, the flow behavior is typically characterized by the Reynolds number, Re, that describes the ratio of inertial to viscous forces and is defined as:

$$Re = \frac{v_c L_c}{\nu_F}, \tag{2}$$

where v_c is the characteristic fluid velocity, such as the free-stream velocity or the fluid velocity at an inlet. In this work the characteristic fluid velocity will be taken as the maximum in the domain, defining a maximum local Reynolds number. The behavior of natural convection flows is better characterized by the Grashof number that describes the ratio of buoyancy to viscous forces and is defined as:

$$Gr = \frac{|\mathbf{g}|\beta \Delta T L_c^3}{\nu_F^2}. \tag{3}$$

Assuming temperature independent fluid properties, the Rayleigh number increases with Grashof number. For low Rayleigh and Grashof numbers and constant boundary conditions, the flow converges to a steady-state. As the

Rayleigh number exceeds a critical value, thermal instabilities emerge and the flow exhibits an unsteady behavior. One example is the flow in a cylinder, its axis aligned with the gravity vector. Holding the top and bottom surfaces at fixed (different) temperatures and assuming adiabatic side walls, for an aspect ratio 1 the flow in the cylinder will exhibit unsteady behavior beginning at Rayleigh numbers of approximately 10^5 (Touihri et al. 1999).

The emergence of instabilities depends on the fluid properties, the boundary conditions, and the geometry of the enclosure as well as internal structures. As the latter evolves during the optimization process, the flow may become unsteady for an intermediate design in the course of the optimization process, while being steady for the initial design. To consider design problems with a large range of Rayleigh and Reynolds' numbers, it is important to describe a potentially unsteady flow behavior and consider the transient response in the formulation of the optimization problem.

2.2 Formulation of design optimization problem

The design problems studied here have a state-dependent objective, such as minimizing the temperature at a given location in the design domain. As the state variables, i.e. temperature, fluid velocity and fluid pressure, may vary in time, the objective function is defined by an integral over a given time period. The design constraints considered in this work only depend on the LSF which is defined by an explicit function of the optimization variables; see Section 3. These constraints are used to regularize the optimization problem and are defined in Section 5 for the particular problems studied here. This class of optimization problems can be written as follows:

$$\begin{aligned} &min_{\mathbf{s}}\ Z = \int_{t_1}^{t_2} z(\mathbf{s}, \mathbf{u}(t))dt, \\ &s.t.\quad g_i(\mathbf{s}) \leq 0 \quad i = 1 \ldots N_g, \\ &\qquad \mathbf{s} \in \mathbf{S} = \left\{ \mathbb{R}^{N_s} | s_i^L \leq s_i \leq s_i^U,\ i = 1....N_s \right\}, \end{aligned} \tag{4}$$

where the objective Z is the integral of the time dependent function z over the time interval $[t_1, t_2]$. The instantaneous function z depends on the vector of optimization variables $\mathbf{s}$ and the vector of state variables $\mathbf{u}$, which may vary in time, t. The N_s optimization variables s_i are bounded by lower and upper limits, s_i^L and s_i^U. The state variables satisfy the governing equations of the natural convection problem which is described in Section 4.1. The number of inequality constraints is denoted by N_g.

3 Parametrization of level set function

The geometry of a solid body immersed in fluid is defined by the LSF, $\phi(\mathbf{x})$, where $\mathbf{x}$ denotes the vector of spatial coordinates. Assuming that the body consists of one solid phase, a single LSF function is sufficient to describe the spatial distribution of the fluid and solid phases as follows:

$$\begin{aligned} &\phi(\mathbf{x}) < 0, \quad \forall\, \mathbf{x} \in \Omega_S, \\ &\phi(\mathbf{x}) > 0, \quad \forall\, \mathbf{x} \in \Omega_F, \\ &\phi(\mathbf{x}) = 0, \quad \forall\, \mathbf{x} \in \Gamma_{FS}, \end{aligned} \tag{5}$$

where Ω_S is the solid phase, Ω_F the fluid phase and Γ_{FS} the fluid-solid interface.

The level set function can be parametrized to describe a combination of geometric primitives or to allow for the evolution of geometries in the optimization process. Both approaches are used in the numerical examples in Section 5 and described in the following subsections. In both cases, the LSF is mapped onto the XFEM mesh by evaluating the parametrized LSF at the nodes. Standard finite element shape functions are used to interpolate the LSF value at a point within an element. Here, bi-linear and tri-linear shape functions are used for 2D and 3D problems, respectively. These shape functions permit that an element edge can be intersected by the fluid-solid interface, i.e. $\phi = 0$, at most once. The lines (2D) and faces (3D) spanned by the edge intersection points, $\mathbf{x}_i^\Gamma$, define the fluid-solid interface within a finite element; see Fig. 1. The phase, i.e. fluid or solid, of the subdomains within the elements is determined by the sign of the level set values of the associated finite element nodes. To this end, we introduce an auxiliary level set function $\bar{\phi}$ such that $\bar{\phi} = -1$ in solid subdomains and $\bar{\phi} = 1$ in fluid subdomains. To avoid numerical issues due to the zero level set iso-contour intersecting finite element nodes, nodal level set values that are close to zero, i.e. $\|\phi_i\| \leq 10^{-8}\ h_e$, are set to $\phi_i = 10^{-8}\ h_e$, where h_e is the size of the finite element. Numerical experiments showed that the

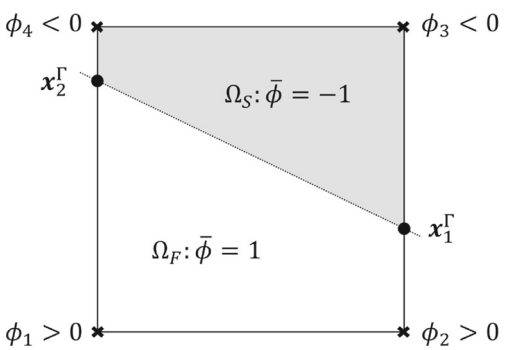

Fig. 1 Construction of interface geometry for intersected elements

influence of this perturbation on the optimization results is imperceptible.

The linear interpolation scheme and the construction of the interfaces restrict the geometry resolution of the LSF to the size of a finite element and may cause convergence issues in the optimization process if sub-element-size features are advantageous. This issue has been discussed in Jenkins and Maute (2015) and Coffin and Maute (2015). A regularization scheme to discourage the formation of sub-element-size features has been recently proposed by the authors and is briefly outlined in Section 3.3.

3.1 Petal geometry

To gain insight into the fundamental characteristics of the class of natural convection problems studied here, we first restrict the set of 2D geometries that can emerge in the optimization process. To this end, we parametrize the LSF such that it describes a radial arrangement of petal-like features. A configuration with three petals is depicted in Fig. 2. The petals are evenly spaced around a semicircle of radius $\tilde{h}_b$. The total petal length is defined by $\tilde{h}_t$ and the petal width by $\tilde{w}_p$, which varies sinusoidally in radial direction with an amplitude $\tilde{a}$. These parameters, i.e. $\tilde{h}_b$, $\tilde{h}_t$, $\tilde{w}_p$, and $\tilde{a}$, can be defined as the optimization variables, s_i, for either each petal individually or uniformly for a group of petals. Note that the petal geometry is defined in non-dimensional form with the height of the design domain being the reference length, i.e. $\mathbf{x} = L_c\tilde{\mathbf{x}}$, where $\tilde{\cdot}$ denotes a non-dimensional parameter.

The petal configuration is defined by the superposition of multiple LSFs, describing the individual petals and the circular base. Each petal is defined in a local coordinate system, $\tilde{\mathbf{x}}'$, that is aligned with the symmetry axis of the petal. The level set value, $\phi(\tilde{\mathbf{x}})$, is defined as:

$$\phi_i(\tilde{\mathbf{x}}) = min_{KS}(\phi_c(\tilde{\mathbf{x}}), \phi_{p,j}(\tilde{\mathbf{x}})), \tag{6}$$

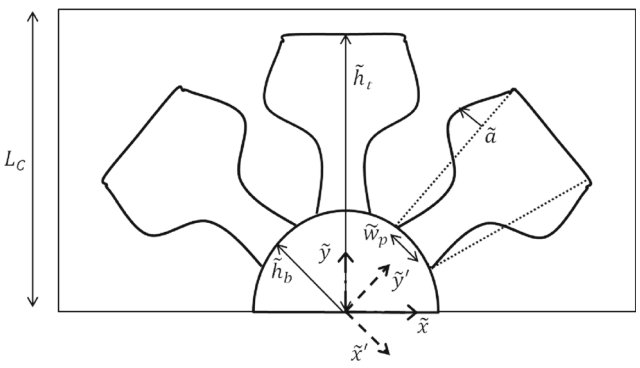

Fig. 2 Configuration of petal design with three petals

where $\phi_{p,j}$ is the LSF of the j-th petal and ϕ_c describes the circular base as:

$$\phi_c = \sqrt{\tilde{x}^2 + \tilde{y}^2} - \tilde{h}_b. \tag{7}$$

The Kreisselmeier-Steinhauser function, min_{KS}, is used to approximate the minimum level set value, ϕ_i, ensuring the differentiability of the formulation with respect to the petal parameters (Kreisselmeier and Steinhauser 1979). This function is defined as:

$$min_{KS}(\phi) = \frac{-1}{\beta} ln \left(\sum_{k=1}^{N_{LS}} e^{-\beta\phi_k} \right), \tag{8}$$

where the minimum level set value of a set of N_{LS} values is computed with a sharpness parameter, β. The j-th petal is described by $\phi_{p,j}$ which defines a cuboid with curved edges:

$$\phi_{p,j} = \left(\left[\frac{2\tilde{x}_x \tilde{h}_b}{\tilde{w}_w} \right]^p + \left[\frac{\tilde{y}_y \tilde{h}_b}{\tilde{h}_p} \right]^p \right)^{\frac{1}{p}}. \tag{9}$$

The sharpness of the corners is controlled by the parameter p and set to 10 in this study. The petal length, $\tilde{h}_p$, is defined as:

$$\tilde{h}_p = \tilde{h}_t - \tilde{h}_b. \tag{10}$$

The width of the cuboid, $\tilde{w}_w$, varies in radial direction, i.e. $\tilde{y}'$, as follows:

$$\tilde{w}_w = \tilde{w}'_p + \frac{\pi}{N_p - 1} \left(\tilde{y}' - \tilde{h}_b \right). \tag{11}$$

Note that the maximum width depends on the number of petals N_p. The axillary coordinates $\tilde{x}_x$ and $\tilde{y}_y$ introduced in (9) are defined as functions of the local coordinates $\tilde{x}'$ and $\tilde{y}'$:

$$\tilde{x}_x = \tilde{x}' - sign\left(-\tilde{x}'\right) \tilde{a}\, \tilde{w}_w\, sin\left(\frac{3}{2}\pi \frac{1}{\tilde{h}_p} \left(\tilde{y}' - \tilde{h}_b \right) \right), \tag{12}$$

$$\tilde{y}_y = \tilde{y}' - \tilde{h}_b. \tag{13}$$

The sine function in (12) defines the curvature of the cuboid edges.

3.2 Topology optimization

To allow for the emergence of a larger set of geometries in the optimization process, the LSF is parametrized by local shape functions defined on a finite element mesh. While this mesh may differ from the XFEM mesh to predict the temperature and flow fields, for simplicity we use the XFEM mesh for parameterizing the LSF in this study.

We assign one optimization variable, $s_i, i = 1 \dots N_n$ to each node of the XFEM mesh, where N_n is the number of nodes. The LSF value of the i-th node, ϕ_i, is defined by an explicit function of the optimization variables as follows:

$$\phi_i = \left(\sum_{j=1}^{N_n} w_{ij} \right)^{-1} \sum_{j=1}^{N_n} w_{ij} s_j, \tag{14}$$

where

$$w_{ij} = max\left(0, (r_f - |\mathbf{x}_i - \mathbf{x}_j|)\right), \tag{15}$$

and r_f is the prescribed filter radius. The filter (14) accelerates the convergence of geometry in the optimization process and may promote (but does not guarantee) smooth shapes of the phase boundaries; see, for example, Kreissl and Maute (2012). Numerical experiments have shown that filter radii of $2.0 - 4.0$ times the element width to yield an effective and efficient smoothing of nodal design variables. Within this range the optimization results do not depend noticeably on choice of r_f.

3.3 Feature size control

To discourage the formation of small, sub-element-size features and to control the slope of the LSF near the fluid-solid interface, we introduce the following measure of the spatial LSF gradients:

$$G = \int e^{-\alpha^2} \left(|\nabla\phi| - d\phi_p \right)^2 d\Omega \quad \text{with } \alpha = e_p \frac{\phi}{\Delta\phi}, \tag{16}$$

where e_p is the penalization parameter, $d\phi_p$ the desired level set gradient, and $\Delta\phi$ the range of the level values in the design domain, defined as:

$$\Delta\phi = \phi_{max} - \phi_{min}. \tag{17}$$

The gradient measure (16) consists of two terms: The first term becomes vanishingly small far from the zero level set contour and unity nearby; the second term is zero when the level set gradient is equal to the desired value. The combination of these two terms penalizes level set gradients that do not match the desired value, $d\phi_p$, along the fluid-solid interface. The value of $d\phi_p$ is typically set to unity to promote uniformly scaled shape sensitives along the phase boundaries; see, for example, Burger and Osher (2005) and van Dijk et al. (2013). This functionality of the gradient measure is similar to the one of re-initialization schemes often used in traditional LSMs, which advance the design via the solution of the Hamilton-Jacobi equation.

The authors have recently shown that the gradient measure (16) can be also used to discourage the formation of sub-element-size featured when combined with properly selected upper and lower bounds on the optimization variables (Coffin and Maute 2015). This concept is illustrated in Fig. 3. Restricting the level set values to $\pm h_{ele}/2$, where h_{ele} is the element size, the minimum feature size is h_{ele} if the gradient of the LSF is one. The reader is referred to Coffin and Maute (2015) for further details. In Section 5, an upper limit on the gradient measure (16) is imposed to regularize the optimization problems.

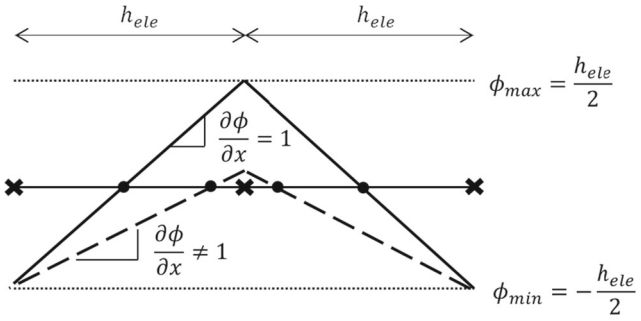

Fig. 3 LSF gradient measure concept, *dotted line* showing insufficient gradient

4 Analysis

The main challenge in optimizing the topology of natural convection problems is the modeling and numerical prediction of the temperature and flow fields. In this section, we present the weak form of the governing equations, outline the spatial and temporal discretization schemes, and summarize the main steps of the adjoint sensitivity analysis.

4.1 Governing equations

In this study, we describe natural convection flows by coupling an advection-diffusion equation, which describes the transport of thermal energy, and the incompressible Navier-Stokes equations, which describe the transport of mass and momentum. The buoyancy forces are modeled by the Boussinesq approximation. While this fluid model is only valid for low Mach number flows, it describes well a broad range of problems relevant for engineering design. The heat transfer in the solid phase is described by a linear diffusion model. Fluid and solid models are coupled at the fluid-solid interface through temperature and heat flux continuity conditions. The residual weak form of the governing equations in the fluid and solid phases are summarized subsequently.

4.1.1 Incompressible Navier-Stokes equations

The residual of the weak form of the incompressible Navier-Stokes equations, R^F, is decomposed into volumetric and surface contributions:

$$R^F = R^F_\Omega + R^F_{stab} + R^F_{\Gamma_{ext}} + R^F_{\Gamma_{FS}} = 0, \tag{18}$$

where R^F_Ω and R^F_{stab} are the residuals of the volumetric non-stabilized and stabilized contributions, $R^F_{\Gamma_{ext}}$ is the residual of contribution from external boundaries, and $R^F_{\Gamma_{FS}}$ is the residual of the fluid-solid interface conditions. The stabilization term, R^F_{stab}, depends on the discretization scheme and is defined in Section 4.2. For the problems considered in this study, the contributions form external boundaries vanish as the fluid velocities are set to zero along the walls enclosing the flow domain.

The non-stabilized volumetric contributions are:

$$\begin{aligned} R^F_\Omega = & \int_{\Omega_F} \Psi_i \rho_F \left(\frac{\partial v_i}{\partial t} + v_j \frac{\partial v_i}{\partial x_j} \right) d\Omega \\ & + \int_{\Omega_F} \frac{1}{2} \left(\frac{\partial \Psi_i}{\partial x_j} + \frac{\partial \Psi_j}{\partial x_i} \right) \sigma_{ij}\,(\mathbf{v}, p)\, d\Omega \\ & + \int_{\Omega_F} \Psi_i \rho_F g_i \left(1 - \beta_F \left[T_F - T_0\right]\right) d\Omega \\ & + \int_{\Omega_F} \eta \frac{\partial v_i}{\partial x_i} d\Omega, \end{aligned} \tag{19}$$

where v_i is the velocity vector, p the pressure, T_F the temperature, and σ_{ij} the stress tensor of the fluid. The vector Ψ_i denotes admissible test functions for the momentum equations, and η is the test function of the incompressibility condition. The gravity acceleration vector is denoted by g_i and T_0 is the reference temperature. In this form the reference temperature drives the magnitude of buoyancy force through the entire domain. In a closed box, the magnitude of reference temperature will lead to changes in the magnitude of mean pressure in the domain and will not impact the fluid flow velocities. The fluid stress is defined as:

$$\sigma_{ij}(\mathbf{v}, p) = -p\delta_{ij} + \mu \left(\frac{\partial v_i}{\partial x_j} + \frac{\partial v_j}{\partial x_i} \right), \tag{20}$$

where μ is the dynamic viscosity of the fluid.

We enforce weakly the stick condition at the fluid-solid interface by a Nitsche's method (Nitsche 1975). The formulation adopted here is described by Schott et al. (2014) and is written as:

$$\begin{aligned} R^F_{\Gamma_{FS}} = & -\int_{\Gamma_{FS}} \Psi_i\ \sigma_{ij}\ (\mathbf{v}, p)\ n^F_j d\Gamma \\ & - \int_{\Gamma_{FS}} \sigma_{ij}\ (\mathbf{\Psi}, \eta) v_i\ n^F_j d\Gamma \\ & + \gamma_F \int_{\Gamma_{FS}} \Psi_i\ v_i\ d\Gamma, \end{aligned} \tag{21}$$

where n^F_j is the normal on the interface pointing into the solid phase and γ^F is a penalty parameter.

4.1.2 Advection-diffusion equation

The energy transport in the fluid phase is described by an advection-diffusion equation. Setting the advective velocity to zero, this equation simplifies to a diffusion equation which is used to model the conduction in the solid phase. Similar to the Navier-Stokes equations discussed previously, the weak form of the advection-diffusion equation is decomposed into volumetric and surface contributions as follows:

$$R^{T_P} = R^{T_P}_\Omega + R^{T_P}_{stab} + R^{T_P}_{\Gamma_{ext}} + R^{T_P}_{\Gamma_{FS}} = 0, \tag{22}$$

where P denotes the phase, i.e. fluid or solid. The stabilized volumetric contribution, $R^{T_P}_{stab}$, is discussed in Section 4.2. The non-stabilized volumetric contribution, $R^{T_P}_\Omega$, is:

$$\begin{aligned} R^{T_P}_\Omega = & \int_{\Omega_P} \zeta_P\ \rho_P\ c_{p,P} \left(\frac{\partial T_P}{\partial t} + v^P_j \frac{\partial T_P}{\partial x_j} \right) d\Omega \\ & + \int_{\Omega_P} \frac{\partial \zeta_P}{\partial x_i}\ J^P_i\ (T_P)\ d\Omega, \end{aligned} \tag{23}$$

where ζ_P is an admissible test function and J^P_i the diffusive heat flux. Note the advective velocity v^P_i is the fluid velocity v_i in $\Omega_k = \Omega_F$ and vanishes in the solid phase. Assuming isotropic diffusion in both fluid and solid phase, the heat flux is:

$$J^P_i\ (T_P) = \kappa_P\ \frac{\partial T_P}{\partial x_i}. \tag{24}$$

The contribution from the external boundaries, $R^{T_P}_{\Gamma_{ext}}$, is due to applied heat surface fluxes and is defined as:

$$R^{T_P}_{\Gamma_{ext}} = \int_{\Gamma^q_P} \zeta_P\ q_P\ d\Gamma, \tag{25}$$

where Γ^q_P denotes the surface of phase P at which the surface flux q_P is applied.

The continuity of the temperature field and the surface fluxes at the fluid-solid interface is enforced weakly using Nitsche's method. Following the work of Dolbow and Harari (2009), the surface contributions $R^{T_F}_{\Gamma_{FS}}$ and $R^{T_S}_{\Gamma_{FS}}$ are defined through the following integrals:

$$\begin{aligned} R^{T_F}_{\Gamma_{FS}} + R^{T_S}_{\Gamma_{FS}} = & -\int_{\Gamma_{FS}} \langle \zeta \rangle\ \{J_i\,(T_F, T_S)\}\ n^F_i\ d\Gamma \\ & - \int_{\Gamma_{FS}} \{J_i\,(\zeta_F, \zeta_S)\}\ n^F_i\ \langle T \rangle\ d\Gamma \\ & + \gamma_T \int_{\Gamma_{FS}} \langle \zeta \rangle\ \langle T \rangle\ d\Gamma, \end{aligned} \tag{26}$$

with

$$\langle z \rangle = z_F - z_S \quad \text{and} \quad \{J_i\,(z_F, z_S)\} = w^F J^F_i(z_F) + w^S J^S_i(z_S), \tag{27}$$

where γ_T is a penalty parameter and w^F and w^S are weights such that $w^F + w^S = 1$.

4.2 Spatial discretization

The governing equations in the fluid and solid phase are discretized in space by the XFEM. The XFEM augments the standard finite element interpolation by additional enrichment functions to capture discontinuities in either the state variables or their spatial gradients within an element. Depending on the type of discontinuity, different enrichment schemes are applied (Fries and Belytschko 2010). The particular approach used in this study is adopted from Makhija and Maute (2014), Kreissl and Maute (2012), Lang et al. (2014), Makhija and Maute (2015), who considered linear elastic, incompressible Navier-Stokes, diffusion, and advection-diffusion problems, respectively.

The XFEM is used to approximate the fluid velocity and pressure fields as well as the temperature fields in the solid and fluid phases within finite elements that are intersected by the fluid-solid interface, i.e. the zero level set iso-contour. With u representing one of these state variables, a Heaviside enrichment strategy is used to discretize the governing equations. The approximation of u within an element, $\hat{u}$, is defined as:

$$\hat{u}(\mathbf{x}) = \sum_{m=1}^{M} \left(H(-\bar{\phi}(\mathbf{x})) \sum_{i \in I} N_i(\mathbf{x})\ \delta_{mk}^{i,F}\ u_{i,m}^{F} + H(\bar{\phi}(\mathbf{x})) \sum_{i \in I} N_i(\mathbf{x})\ \delta_{mn}^{i,S}\ u_{i,m}^{S} \right) \tag{28}$$

where I is the set of all elemental nodes, $N_i(\mathbf{x})$ the nodal basis functions, M the number of enrichment levels, and $u_{i,m}^{F}$ and $u_{i,m}^{S}$ are the degrees of freedom of enrichment level m at node i in the fluid and solid phases, respectively. To satisfy the partition of unity principle, no more than one degree of freedom per node is used to interpolate the solution at a point in the element. The active degrees of freedom at the i-th node are denoted by k and n in fluid and solid phases, respectively, and $\delta_{ab}^{i,P}$ for $P = [F, S]$ is the Kronecker delta. The Heaviside function, $H(z)$, turns on and off the interpolation for the particular phase and is defined as:

$$H(z) = \begin{cases} 1 & z > 0 \\ 0 & z \leq 0 \end{cases}. \tag{29}$$

For each phase, multiple enrichment levels, i.e. sets of shape functions, may be necessary to interpolate the state variables in multiple, physically disconnected regions of the same phase; see Makhija and Maute (2014), Terada et al. (2003), and Tran et al. (2011). This generalization prevents spurious coupling between disconnected regions of the same phase. The reader is referred to Makhija and Maute (2014) for details of the particular approach used here. To accurately integrate the weak form of the static equilibrium equations by Gauss quadrature, intersected elements are decomposed into triangles in 2D and tetrahedrons in 3D.

The convective terms in the incompressible Navier-Stokes and advection-diffusion equations may cause spurious node-to-node velocity oscillations. Furthermore, we interpolate both the fluid velocity and pressure by bi-linear shape functions in 2D and tri-linear shape functions in 3D. This equal-order interpolation gives rise to spurious pressure oscillations. To prevent these numerical instabilities, we augment the incompressible Navier-Stokes by the Streamline Upwind Petrov Galerkin (SUPG) and Pressure Stabilized Petrov Galerkin (PSPG) stabilization (Tezduyar et al. 1992), yielding the following volumetric contribution to (18):

$$R_{stab}^{F} = \sum_{e=1}^{N_e^F} \int_{\Omega_{F,e}} \left(\tau_{SUPG}^{v}\ v_j\ \frac{\partial \Psi_i}{\partial x_j} + \frac{1}{\rho_F}\ \tau_{PSPG}\ \frac{\partial \eta}{\partial x_i} \right) \left(\rho_F \left(\frac{\partial v_i}{\partial t} + v_j\ \frac{\partial v_i}{\partial x_j} \right) - \frac{\partial \sigma_{ij}(\mathbf{v}, p)}{\partial x_j} + \rho_F\ g_i\ (1 - \beta_F\ [T_F - T_0]) \right) d\Omega, \tag{30}$$

where N_e^F denotes the number of elements in the fluid phase. The stabilization parameters τ_{SUPG}^{v} and τ_{PSPG} are given by Tezduyar et al. (1992). The advection-diffusion equation in the fluid phase is stabilized by the following SUPG term:

$$R_{stab}^{T_F} = \sum_{e=1}^{N_e^F} \int_{\Omega_{F,e}} \frac{\tau_{SUPG}^{T}}{\rho_F\ c_{p,F}}\ v_i \frac{\partial \zeta}{\partial x_i} \times \left(\rho_F\ c_{p,F} \left(\frac{\partial T_F}{\partial t} + v_i \frac{\partial T_F}{\partial x_i} \right) - \frac{\partial J_i^F}{\partial x_i} \right) d\Omega, \tag{31}$$

where the stabilization parameter τ_{SUPG}^{T} is defined in Franca et al. (1992).

4.3 Time integration scheme

The XFEM discretization yields the following semi-discrete form of the governing equations:

$$\mathbf{R}_u(\mathbf{u}, \dot{\mathbf{u}}) = \mathbf{0}, \tag{32}$$

where the vector $\mathbf{u}$ collects the degrees of freedom of the fluid velocity, pressure, and temperature fields, as well as the temperature field in the solid; its time derivative is denoted by $\dot{\mathbf{u}}$. We discretize the governing equations in time by an implicit Euler backward scheme:

$$\dot{\mathbf{u}}^{(n)} = \frac{\mathbf{u}^{(n)} - \mathbf{u}^{(n-1)}}{\Delta t^{(n)}}, \quad n = 1 \ldots N_t, \tag{33}$$

where n is the time index, $\Delta t^{(n)}$ the time step size, and N_t the number of time steps.

At time step $n = 0$, the initial conditions, $\mathbf{u}_0$, are satisfied for all state variables such that:

$$\mathbf{R}_u^{(0)} = \mathbf{u}^{(0)} - \mathbf{u}_0. \tag{34}$$

For all time steps $n > 0$, the equilibrium at the time step (n) is satisfied by solving the nonlinear system $\mathbf{R}_u^{(n)} = \mathbf{0}$ via Newton's method. To this end the system is linearized at $\mathbf{u}^{(n)}$, yielding the following contributions to the Jacobian:

$$\mathbf{J}_{u^{(n)}}^{(n)} = \frac{\partial \mathbf{R}_u^{(n)}}{\partial \mathbf{u}^{(n)}}\bigg|_{u^{(n)}} + \frac{\partial \mathbf{R}_u^{(n)}}{\partial \dot{\mathbf{u}}^{(n)}}\bigg|_{u^{(n)}} \frac{1}{\Delta t^{(n)}} \tag{35}$$

Note that due to the SUPG and PSPG stabilization terms, the second term in the above equation depends on the solution $\mathbf{u}^{(n)}$. We compute the derivatives in (35) based on the analytically differentiated finite element formulations.

4.4 Sensitivity analysis

The objective functions considered in this study can be written in discretized form as:

$$Z = \sum_{n=N_t^1}^{N_t^2} z^{(n)}\left(\mathbf{s}, \mathbf{u}^{(n)}\right), \tag{36}$$

where the time steps N_t^1 and N_t^2 correspond to the times interval $[t_1, t_2]$ defined in (4). The derivatives of the objective function with respect to the optimization variables are computed by the adjoint method. To this end, we adopt the discrete formulation for nonlinear fluid and coupled systems of Kreissl and Maute (2011) and Golmon et al. (2012). The main steps of the computational procedure are summarized subsequently.

The derivative of the objective function with respect to the optimization variable s_i is decomposed into an explicit and an implicit term such that:

$$\frac{dZ}{ds_i} = \frac{\partial Z}{\partial s_i} + \sum_{n=N_t^1}^{N_t^2} \frac{\partial z^{(n)}}{\partial \mathbf{u}^{(n)}}^T \frac{\partial \mathbf{u}^{(n)}}{\partial s_i}. \tag{37}$$

The explicit term is evaluated by differentiating Z first with respect to the nodal level set values, ϕ_j. For convenience these derivatives are evaluated by finite differences. The resulting vector, $(\partial Z/\partial \phi_j)$, is then post-multiplied by the derivative of the nodal level set values with respect to the optimization variables, $(\partial \phi_j/\partial s_i)$, differentiating the explicit expressions introduced in Sections 3.1 and 3.2. The same procedure is used to compute the derivatives of the constraints in (4), as they do not depend on the state variables in this study.

The implicit term in (37) is computed by the adjoint method as follows:

$$\sum_{n=N_t^1}^{N_t^2} \frac{\partial z^{(n)}}{\partial \mathbf{u}^{(n)}}^T \frac{\partial \mathbf{u}^{(n)}}{\partial s_i} = \sum_{n=0}^{N_t^2} \lambda^{(n)^T} \frac{\partial \mathbf{R}_u^{(n)}}{\partial s_i}, \tag{38}$$

where $\lambda^{(n)}$ are the adjoint states at time step n. Note that the scalar product of the adjoint vector and the derivative of the residual $\mathbf{R}_u^{(n)}$ is summed from the initial time step through $n = N_t^2$. The adjoint state are computed by integrating the adjoint equations backward in time as follows:

$$\left(\mathbf{J}_{u^{(n)}}^{(n)}\right)^T \lambda^{(n)} = -\frac{\partial z^{(n)}}{\partial \mathbf{u}^{(n)}} + \frac{1}{\Delta t^{(n+1)}} \frac{\partial \mathbf{R}_u^{(n+1)}}{\partial \dot{\mathbf{u}}^{(n+1)}}\bigg|_{u^{(n+1)}}^T \lambda^{(n+1)}, \tag{39}$$

for $n = N_t^2 \ldots 0$ and $\lambda^{(N_t^2+1)} = \mathbf{0}$. In this work, we compute the derivative of the objective function components with respect to the state variables, $\partial z^{(n)}/\partial \mathbf{u}^{(n)}$, analytically. The derivatives of the residual with respect to the design variables, $\partial \mathbf{R}_u^{(n)}/\partial s_i$, are computed by finite difference. Note that only the residuals of intersected elements need to be considered as the derivatives of non-intersected elements vanish.

The differentiation of the residual of intersected elements with respect to the optimization variables deserves particular attention. The derivative of an elemental residual, R_e^n, at time step n can be conveniently decomposed as follows:

$$\frac{\partial R_e^n}{\partial s_i} = \sum_{j=1}^{N_n^e} \sum_{k=1}^{N_n^\Gamma} \frac{\partial R_e^n}{\partial \mathbf{x}_k^\Gamma} \frac{\partial \mathbf{x}_k^\Gamma}{\partial \phi_j} \frac{\partial \phi_j}{\partial s_i}, \tag{40}$$

where N_n^e is the number of nodes and N_n^Γ the number of intersection points per element. The first term in the double sum of (40) describes the change of the elemental residual due to a change in the interface geometry which is defined by the position, $\mathbf{x}_k^\Gamma$, of the intersection points along the element edges; see Section 3. The second term represents the dependence of $\mathbf{x}_k^\Gamma$ on the level set value, ϕ_j, at the finite element nodes. The last term captures the explicit dependence of ϕ_j on the optimization variables. The decomposition (40) illustrates clearly that the proposed LSM essentially uses shape derivatives to update the design in the optimization process.

Assuming that $\phi_j(s_i)$ is smooth, the partial derivatives in (40) exist for all values of s_i, except for $\phi_j = 0$. In this case, for an infinitesimal perturbation of ϕ_j, edge intersection points may emerge or vanish and a subset of degrees for freedom, $u_{i,m}^P$ with $P = [F, S]$, may become active or inactive, as defined by the Kronecker delta, $\delta_{ab}^{i,P}$, in (28). To mitigate these issues, we construct the nodal level set values such that $\|\phi_j\| > 0$; see Section 3. Furthermore, we evaluate the derivative $\left(\partial R_e^n/\partial \mathbf{x}_k^\Gamma \cdot \partial \mathbf{x}_k^\Gamma/\partial \phi_j\right)$ in the direction which does not alter the sign of ϕ_j. In this work, we compute $\left(\partial R_e^n/\partial \mathbf{x}_k^\Gamma \cdot \partial \mathbf{x}_k^\Gamma/\partial \phi_j\right)$ by a finite difference method. If the sign of a nodal level set value does change due to perturbation $\pm\Delta\phi_j$, a central difference scheme is chosen; otherwise a forward or backward difference scheme is used, depending on the perturbation direction that does not yield

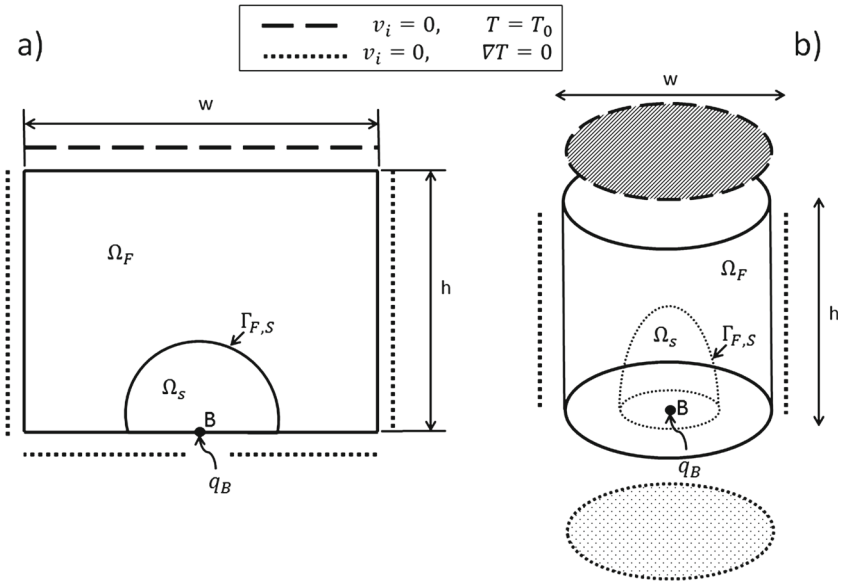

Fig. 4 Configurations of the design problem in **a** two and **b** three dimensions

a sign change. Numerical studies for a broad range of problems rendered this finite differencing approach sufficiently accurate and computationally efficient.

5 Example problems

In this work we study the characteristics of the proposed LSM approach for steady-state problems in 2D and 3D. A transient problem is studied in 2D only due to constraints on computational resources.

The configurations of the 2D and 3D design problems are shown in Fig. 4. In 2D the design domain is a rectangle of width w and height h. In 3D a cylinder of diameter w and height h forms the design domain. In both configurations, a heat flux q_B is applied at point B which is guaranteed to be surrounded by a sphere of solid phase with radius r_{BS}. The temperature on the top surface of the design domains is fixed to T_0. The side and bottom walls are adiabatic. The fluid velocity at the walls and the fluid-solid interface is zero. We assume the properties of air for the fluid phase and the ones of aluminum for the solid phase. The material parameters are summarized in Table 1. The magnitude of the heat flux and the dimensions of the design domains are varied to yield either a steady-state or transient flow response.

The goal of the design problem is to find the geometry of an internal solid structure such that the average temperature at point B, T_B, within the time $[t_1, t_2]$ is minimum. To prevent the trivial solution of an all solid design domain, the volume of the solid phase, V_S, is constrained to be less than or equal to a maximum volume, c_v. To promote smooth shapes and to discourage the formation of small geometric features, we impose a constrained on the perimeter, with c_{pe} denoting the maximum feasible perimeter. To suppress the formation of sub-element-size features, we also impose a constraint on the level set gradient measure described in Section 3.3, with c_g being the upper limit. This optimization problem can be written as follows:

$$
\begin{aligned}
&min_{\mathbf{s}} \; Z = \frac{1}{N_t^{12}} \sum\nolimits_{n=N_t^1}^{N_t^2} T_B^{(n)}, \\
&\text{s.t.} \quad V_S - c_v \leq 0 \\
&\qquad P - c_{pe} \leq 0 \\
&\qquad G - c_g \leq 0 \\
&\qquad \mathbf{s} \in \mathbf{S} = \left\{ \mathbb{R}^{N_s} | s_i^L \leq s_i \leq s_i^U, \; i = 1....N_s \right\}, \qquad (41)
\end{aligned}
$$

Table 1 Material properties for example problems

Property	Value
Gravity	$g = 9.81 \frac{m}{s^2}$
Volumetric thermal expansion	$\alpha_{TE} = 3.43 \times 10^{-3} \frac{1}{K}$
Fluid dynamic viscosity	$\mu_F = 1.511 \times 10^{-5} Pa \cdot s$
Fluid density	$\rho_F = 1.205 \frac{kg}{m^3}$
Fluid specific heat	$c_{p,F} = 1005.0 \frac{J}{kgK}$
Fluid diffusivity	$\kappa_F = 0.0257 \frac{W}{mK}$
Solid density	$\rho_S = 2700.0 \frac{kg}{m^3}$
Solid specific heat	$c_{p,S} = 910.0 \frac{J}{kgK}$
Solid diffusivity	$\kappa_S = 237.0 \frac{W}{mK}$
Reference temperature	$T_0 = 1.0K$

where $N_t^{12} = N_t^2 - N_t^1$ is the number of time steps in the time interval of interest. For steady-state problems, $N_t^{12} = 1$. Numerical studies have shown that the constraint on the gradient measure is only needed for the 3D problem considered here. Therefore, this constraint is omitted for the 2D problems.

The design domains are discretized in space by bilinear quadrilateral elements (2D) and hexahedral, trilinear elements (3D). To enforce the stick condition at the fluid-solid interface we set the fluid penalty parameter to $\gamma_F = 10^4$; see (21). To enforce the temperature continuity the temperature penalty parameter is set to $\gamma_T = 100.0$ and the flux averaging weights to $w^S = w^F = 0.5$; see (26) and (27). For the transient case, the flow and temperature fields are advanced in time by an implicit Euler backward scheme; see Section 4.3. The resulting systems of nonlinear residual equations are solved by a damped Newton-Raphson method. The linear sub-problems of both the forward and the sensitivity analysis are solved by either a sequential or parallel direct solvers, depending on the problem size. We use UMFPACK for 2D problems and MUMPS for the 3D problem (Davis 2004; Amestoy et al. 1998).

The Globally Convergent Method of Moving Asymptotes (GCMMA) of Svanberg (2002) is used to solve the optimization problem. The GCMMA parameters are: relative step size, 0.01; minimum asymptote adaptivity, 0.5; initial asymptote adaptivity, 0.7; maximum adaptivity, 1.43; and constraint penalty, 50. The optimization problem is considered converged if the change of the objective function relative to the initial objective value is less than 10^{-6} and the constraints are satisfied.

The numerical studies presented in the remainder of this section are organized as follows: First we study a steady-state configuration in 2D, restricting the design freedom to a petal geometry. This study illustrates the influence of imposing symmetry conditions on the design. The same configuration is considered with a finite element discretization of the level set function, illustrating the influence of the increased design freedom and the choice of the initial design. A 2D configuration yielding unsteady flow is then considered to understand the influence of a sup-critical Grashof number on the resulting design geometry. Finally, a 3D steady state design problem is considered.

To characterize the flow and temperature fields of the initial and optimized designs, we report on the Rayleigh and Grashof numbers as well as on the maximum local Reynolds number. The domain height is used as the characteristic length, L_c; the maximum difference between the temperature at the top surface and at point B, i.e. $T_B - T_0$, over all time steps is used as characteristic temperature difference, ΔT. The local Reynolds number is computed with respect to the maximum local fluid velocity, i.e. $v_c = max_{\Omega_F}|\mathbf{v}|$.

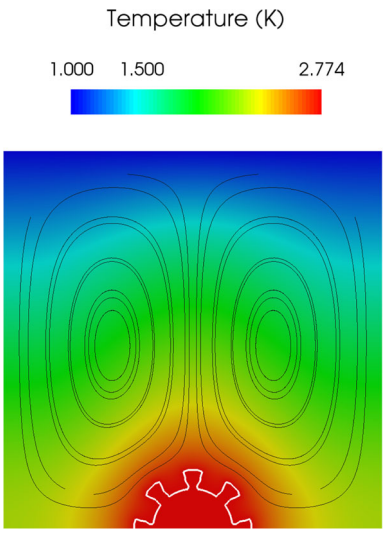

Fig. 5 Initial design for 2D petal geometry optimization

5.1 2D petal geometry optimization

First, we restrict the design freedom to the petal geometry described in Section 3.1 and perform parametric optimization to understand the main characteristics of the design problem. In particular, we study the influence of imposing symmetry conditions on the design. To this end, we consider three variations of a 5-petal layout. In option O1, we enforce the same geometry for each individual petal yielding a total of four optimization variables: $\tilde{h}_b$, $\tilde{h}_t$, $\tilde{w}_p$ and $\tilde{a}$. For option O2, we only enforce symmetry about the vertical axis. Using a uniform base height for all petals, option O2 yields $1 + 3 \times 3$ optimization variables. Finally, in option O3, each petal is allowed a unique geometry, yielding $1 + 5 \times 3$ optimization variables. The initial design for all configurations is shown in Fig. 5. The initial values and the upper and lower bounds of the design parameters are given in Table 2. Note that these bounds allow the petals to overlap and thus the topology to change in the optimization process.

Table 2 Initial values and bounds of design parameters for 2D petal geometry optimization

Parameter	Initial	Minimum	Maximum
Base length, $\tilde{h}_b$	0.21	0.15	0.25
Total length, $\tilde{h}_t$	0.31	0.0	0.9
Petal width, $\tilde{w}_p$	0.21	0.0	0.9
Side variation, $\tilde{a}$	0.0	−0.4	0.4

Table 3 2D optimization parameters

Parameter	Value
Domain height	$h = 0.030\ m$
Domain width	$w = 0.030\ m$
Number of elements	$80 \times 80 = 6400$
Heat flux	$q_B = 5.000 \times 10^{-2} W$
Volume constraint	$c_v = 3.93 \times 10^{-5}\ m^3$
Perimeter constraint	$c_{pe} = 3.14 \times 10^{-2}\ m^2$

The dimension of the design domain and the magnitude of the heat flux is chosen such that a stable steady-solution of the natural convection problem exists throughout the optimization process. At the initial design, the Rayleigh number is $Ra = 6,050$, the Grashof number $Gr = 10,200$, the maximum local Reynolds number $Re_{max} = 10.0$. The problem parameters are summarized in Table 3.

Temperature contour plots with stream lines of the final designs of the three options O1-3 are shown in Fig. 6. The temperatures at point B, the volume, and the perimeter of the optimized designs are given in Table 4. The diffusive and convective contribution to the total heat transport are shown in Fig. 7. The diffusive flux, J^{diff}, in the fluid domain is defined as:

$$J_i^{diff} = -\kappa_F \frac{\partial T}{\partial x_i}, \tag{42}$$

while the advective flux, q^{adv}, is defined as:

$$J_i^{adv} = c_{p,F} \rho_F \ \Delta T v_i, \tag{43}$$

where ΔT is the difference between the local, T, and reference, T_0, temperatures.

Since the convective flux increases with the area of the fluid-solid interface, the perimeter of all designs is either equal or close to the maximum feasible value. Similarly, the designs take up (almost) all of the allowable solid volume in order to extend the solid phase toward the cold top surface. As expected, the objective improves, i.e. the temperature T_B decreases, with increasing design freedom. Option O3 takes advantage of the design freedom and yields an asymmetric design, although the setup of the design problem is symmetric. Comparing the heat flux contributions of the optimized designs suggests that the asymmetric design solution increases in particular the convective energy transport. The differences in convective flux are also reflected in the differences in the flow velocities shown in Fig. 8. As the Rayleigh number of the problem is lowered the benefits from an asymmetric design decrease and the optimization process converges to a symmetric design. This tendency was observed when lowering the product $(\rho_F \ c_{p,F})$ by a factor 1000.0; the results of this study are not shown here as they do not provide fundamentally new insights.

5.2 2D steady-state topology optimization

We consider the same steady-state configuration of Section 5.1 but now study a finite element parameterization of the level set function; see Section 3.2. We compare the optimization results for a symmetric and non-symmetric problem setup. To study the influence of the initial design on the optimization results, we consider the two initializations of the level set function shown in Fig. 9: one consisting of a simple half-circle of radius 0.005, the second imposing a grid of cuboid fluid inclusions over the same solid circle.

The problems parameters are given in Table 3. The radius of the circle of solid phase around point B is $r_{BS} = 10^{-3}\ m$. The smoothing radius of the linear filter (15) is $r_f = 1.440 \times 10^{-3}\ m$. To enforce a symmetric design we define

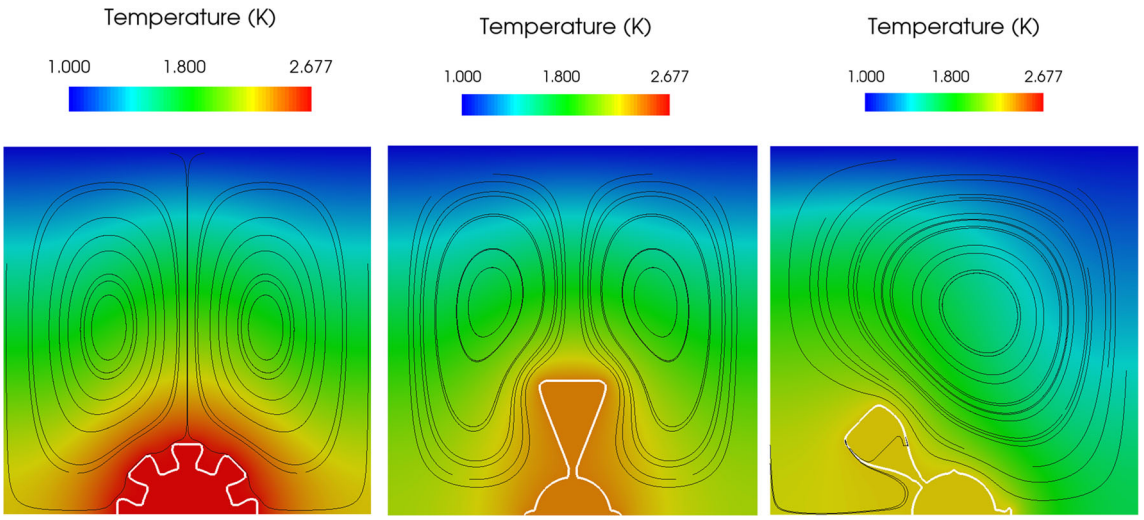

Fig. 6 Temperature contour plots with streamlines of the final designs for petal geometry optimization: option O1 (*left*), O2 (*middle*), O3 (*right*)

Table 4 2D petal geometry optimization results

Design	Initial design	Option O1 - Final design	Option 02 - Final design	Option O3 - Final design
$T_B\ [K]$	2.77	2.68	2.43	2.29
Volume $[m^3]$	2.22×10^{-5}	3.81×10^{-5}	3.93×10^{-5}	3.92×10^{-5}
Perimeter $[m^2]$	2.44×10^{-2}	3.14×10^{-2}	3.14×10^{-2}	3.12×10^{-2}
Rayleigh	6.05×10^{3}	5.72×10^{3}	4.89×10^{3}	4.39×10^{3}
Grashof	1.02×10^{4}	9.68×10^{3}	8.27×10^{3}	7.44×10^{3}
Local Reynolds	1.00×10^{1}	7.78	4.92	1.68×10^{1}

the nodal level set functions at corresponding nodes by the same optimization variables.

For the initial half-circle design the Rayleigh number is $Ra = 5,900$, the Grashof number $Gr = 9,900$, and the maximum local Reynolds number $Re_{max} = 9.0$; for the half-circle with inclusions the Rayleigh number is $Ra = 6,000$, the Grashof number $Gr = 10,000$, and the maximum local Reynolds number $Re_{max} = 9.6$. The values are indicative of a steady state flow for the initial designs.

Figure 10 shows temperature contour plots with streamlines of the optimized designs for the different initial designs and design symmetry conditions. Values for the

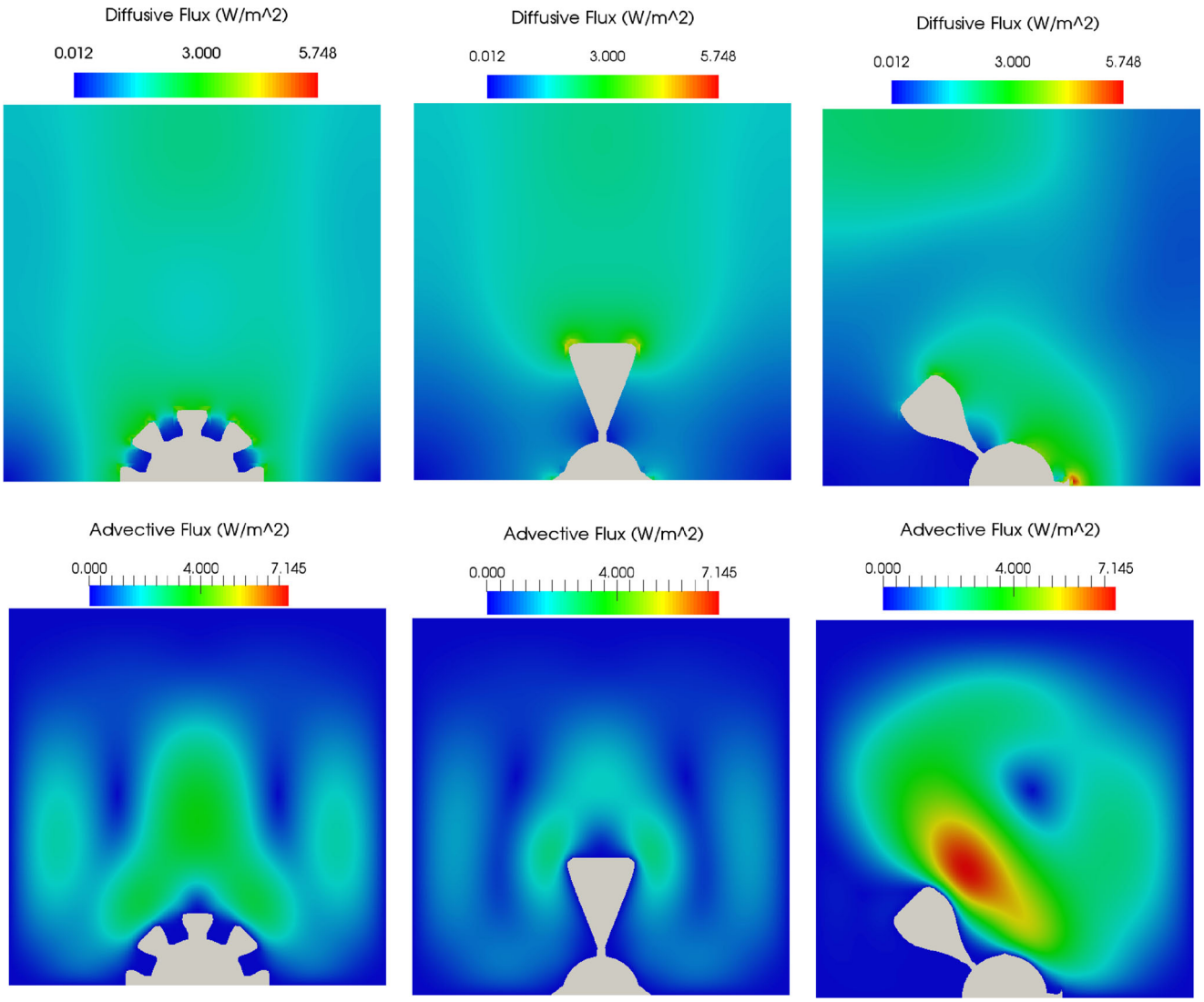

Fig. 7 Diffusive (*top*) and advective (*bottom*) fluxes for petal geometry optimization: option O1 (*left*), O2 (*middle*), O3 (*right*)

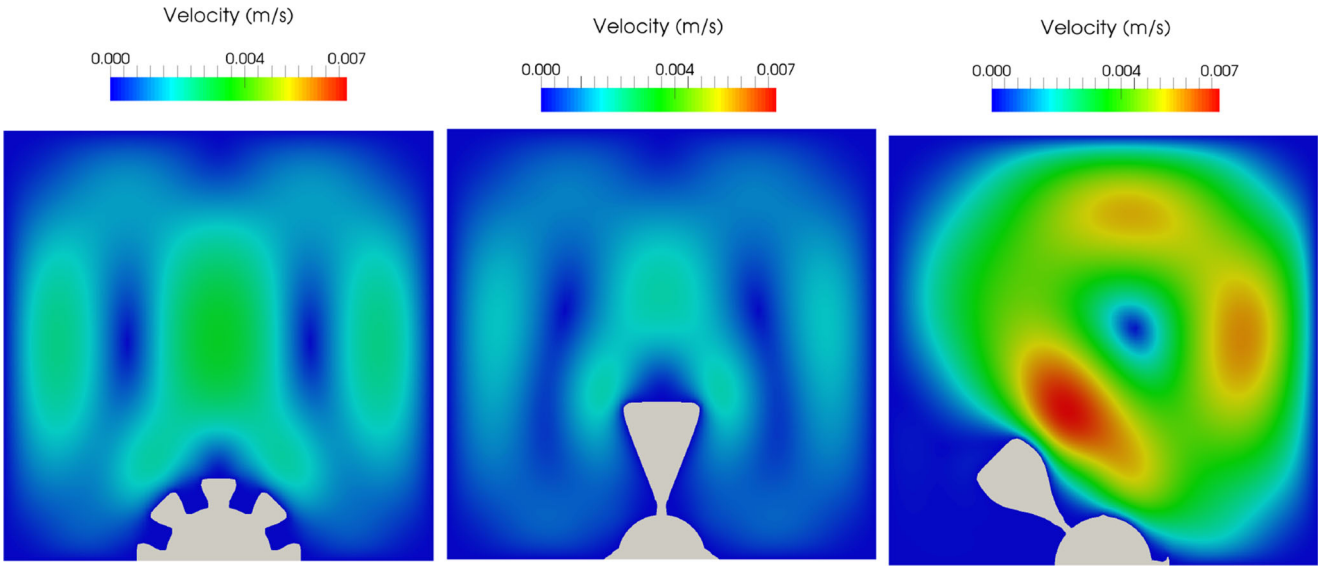

Fig. 8 Magnitude of fluid velocities for petal geometry optimization: option O1 (*left*), O2 (*middle*), O3 (*right*)

temperature T_B, solid volume, and perimeter are given in Tables 5 and 6. Independent of the initial design the optimization process converges to equivalent solutions. Similar to the petal problem studied above, the asymmetric design yields the lowest objective temperature. Again, the asymmetric design features substantially higher advective heat transport due to large flow velocities above the solid structure; see Figs. 11 and 12.

5.3 2D transient topology optimization

Ensuring a steady-state flow for all designs throughout the optimization process imposes severe limitations on the class of optimization problems that can be considered. The proposed optimization framework allows for problems where the flow exhibits a transient response. To illustrate this capability, we consider a configuration similar to the one studied previously, but we increase the magnitude of the external heat flux by a factor 1,000 and the dimensions of the design domain threefold. These modifications cause the flow to exhibit dynamic instabilities. Starting from a design domain of temperature T_0 and the fluid being at rest, the transient analysis is advanced in time until the temperature at point B reaches a quasi-steady-state, i.e. the temporal variations are much smaller than the average. Note the flow remains unstable and does not converge to a steady-state. The objective is the temperature averaged over the last N_t^{12} time steps.

We parameterize the level set function by the XFEM mesh and enforce a symmetric design by defining the nodal

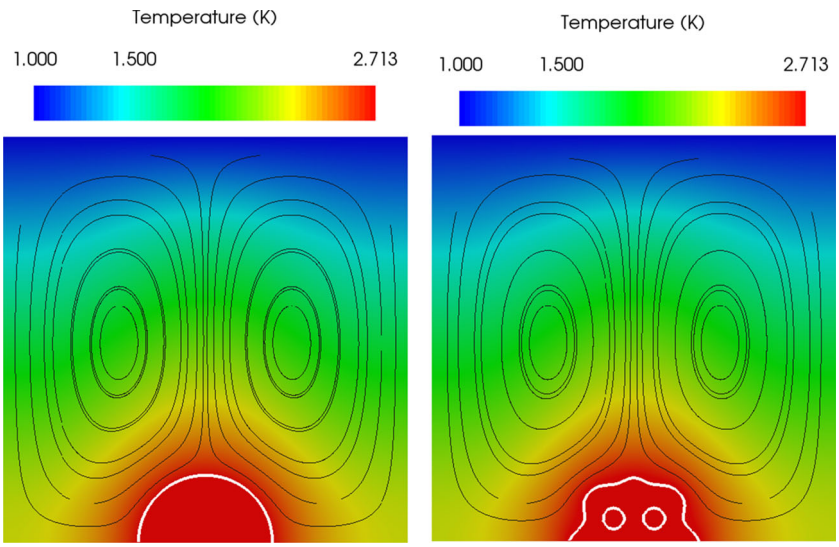

Fig. 9 Temperature contour plots with streamlines of initial designs for 2D steady-state topology optimization: circular (*left*) and inclusions (*right*)

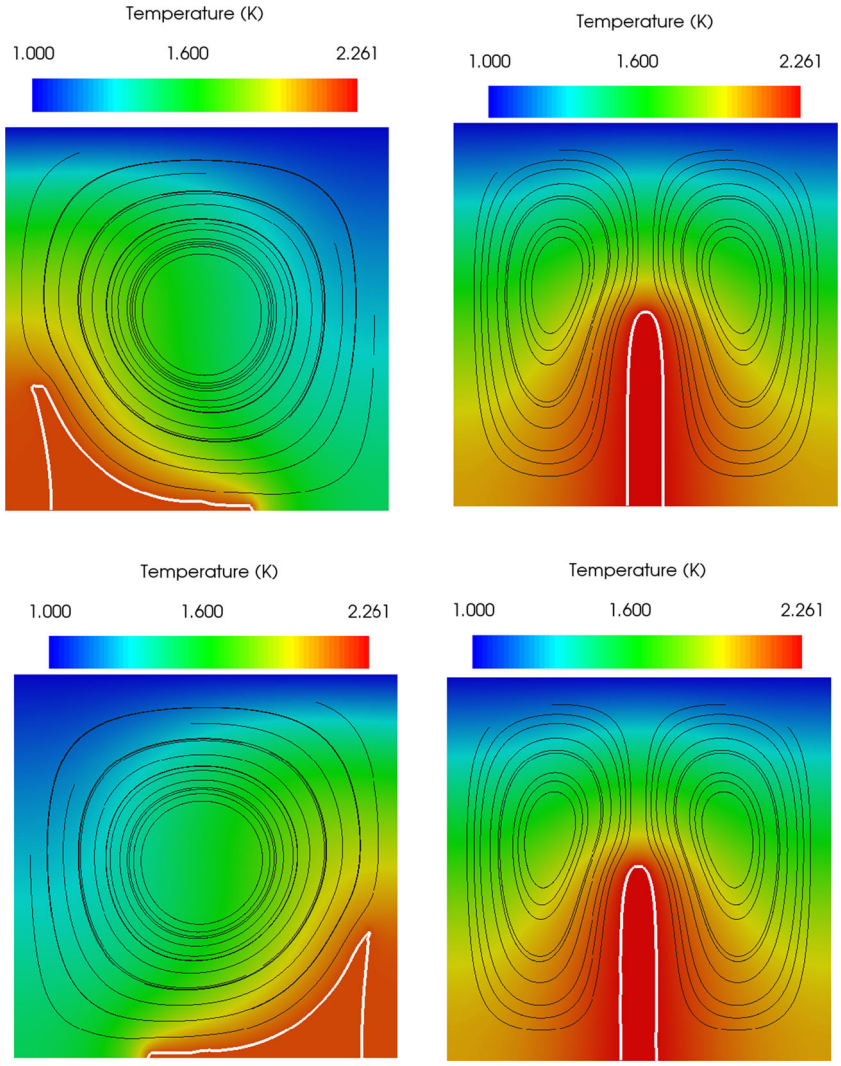

Fig. 10 Temperature contour plots with streamlines of the final designs for 2D steady-state topology optimization: circular initial design (*top*), inclusion initial design (*bottom*); free geometry (*left*), symmetric geometry (*right*)

level set functions at corresponding nodes by the same optimization variables. The smoothing radius of the linear filter (15) is $r_f = 1.44 \times 10^{-3} m$. As in the previous topology optimization study, the radius of the circle of solid phase around point B is $r_{BS} = 10^{-3}\ m$. The upper limits for the volume and perimeter constraints also remain the same.

The problem parameters are summarized in Table 7. Note the large number of time steps needed to reach a quasi-steady-state response at point B. This is due to the significantly different time scales dominating the flow field and the thermal response in the solid. The time step size is driven by the requirement to resolve the transient fluid response

Table 5 2D steady-state topology optimization results for circular initial design

Design	Initial design	Final design (symmetric)	Final design (non-symmetric)
$T_B\ [K]$	2.71	2.26	2.16
Volume $[m^3]$	3.87×10^{-5}	3.93×10^{-5}	3.93×10^{-5}
Perimeter $[m^2]$	1.56×10^{-2}	3.14×10^{-2}	3.14×10^{-2}
Rayleigh	5.85×10^{3}	4.30×10^{3}	3.96×10^{3}
Grashof	9.90×10^{3}	7.27×10^{3}	6.70×10^{3}
Local Reynolds	8.99	5.27	1.85×10^{1}

Table 6 2D steady-state topology optimization results for initial design with inclusions

Design	Initial design	Final design (symmetric)	Final design (non-symmetric)
$T_B\ [K]$	2.75	2.26	2.16
Volume $[m^3]$	2.84×10^{-5}	3.93×10^{-5}	3.92×10^{-5}
Perimeter $[m^2]$	2.52×10^{-2}	3.14×10^{-2}	3.14×10^{-2}
Rayleigh	5.99×10^{3}	4.30×10^{3}	3.95×10^{3}
Grashof	1.01×10^{4}	7.27×10^{3}	6.69×10^{3}
Local Reynolds	9.55	5.27	1.83×10^{1}

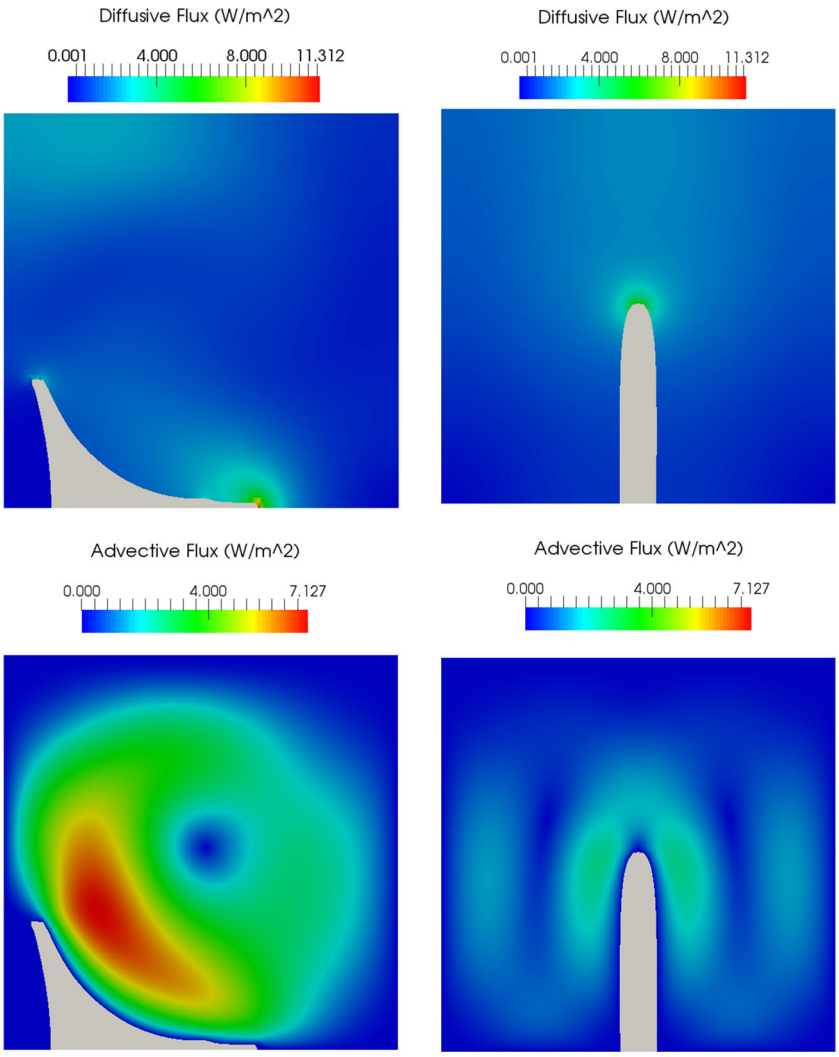

Fig. 11 Advective (*bottom*) and diffusive (*top*) of non-symmetric (*left*) and symmetric (*right*) designs

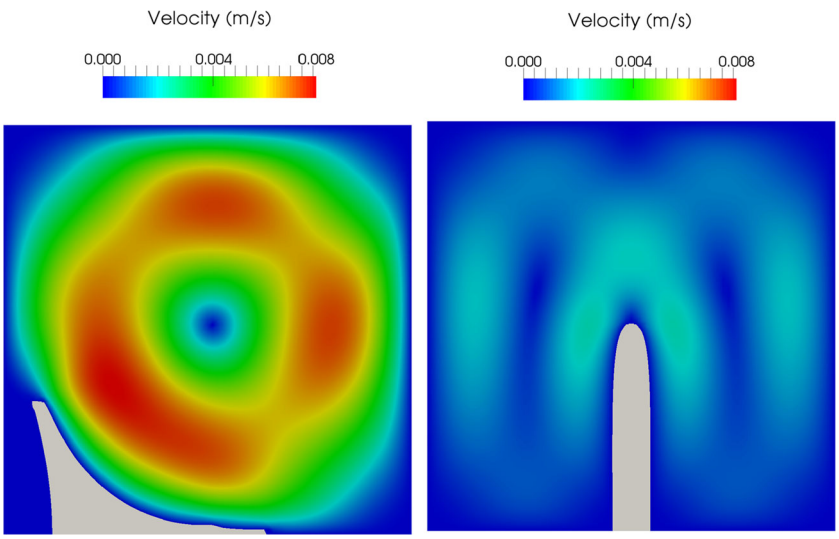

Fig. 12 Magnitude of fluid velocities of non-symmetric (*left*) and symmetric (*right*) designs

Table 7 2D transient topology optimization parameters

Parameter	Value
Domain height	$h = 0.090\ m$
Domain width	$w = 0.090\ m$
Number of elements	6400
Heat flux	$q_B = 5.0 \times 10^1 W$
Volume constraint	$c_v = 3.93 \times 10^{-5}\ m^3$
Perimeter constraint	$c_{pe} = 3.14 \times 10^{-2}\ m^2$
Time step size	$\Delta t = 1.0\ s$
Total number of time steps	$N_t^2 = 2.5 \times 10^3$
Number of averaging time steps	$N_t^{12} = 100$

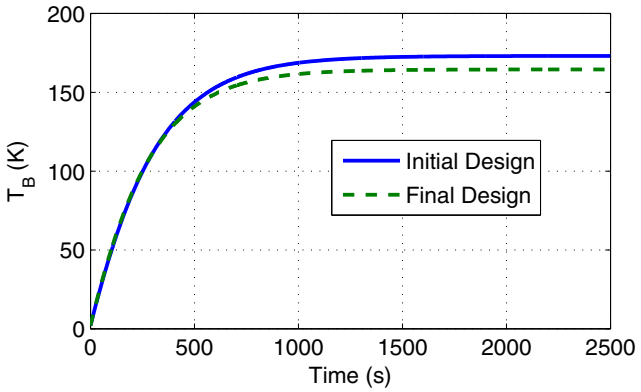

Fig. 14 Temperature T_B plotted over time for initial and final designs of 2D unsteady topology optimization problem

while the total simulation time needs to be sufficiently large such that temperature field in the solid converges. The appropriate time steps size, Δt, the total number of time steps, N_t^2, and the number of time steps for averaging the objective temperature, N_t^{12}, were determined through numerical studies on the initial design.

To reduce the computational effort, we initialize the level set field with the symmetric design found for the steady-state case described previously. Snapshots of the temperature contours with stream lines of the initial and optimized designs are shown in Fig. 13. For the both designs the flow develops a long, thin column that oscillates horizontally as the vortices at the top of the design domain move up and down. While the initial and optimized designs have the same topology, the transient optimum features a more bulbous tip compared to straight fin obtained for the low Grashof number, steady-state design.

The evolutions of the temperature at point B are shown in Fig. 14 for the initial and final designs. For both configurations, the temperature reaches a quasi-steady-state. The average temperature at point B, the solid volume, the perimeter and the non-dimensional numbers characterizing the flow fields of the initial and final designs are given in Table 8. Note that the Rayleigh and Grashof numbers for the initial and optimized design are indicative of an unstable, transient flow.

The transient optimum reduces the mean temperature by 7 % in comparison to the steady-state design which is optimized at much lower Grashof number. Analyzing the design optimized for the transient case at the configuration defined in Section 5.2, which yields a steady-state flow, the objective temperature is $T_B = 2.26\ K$ which is 0.2 % larger than the one of the symmetric steady-state design. This analysis illustrates the importance of optimizing the design

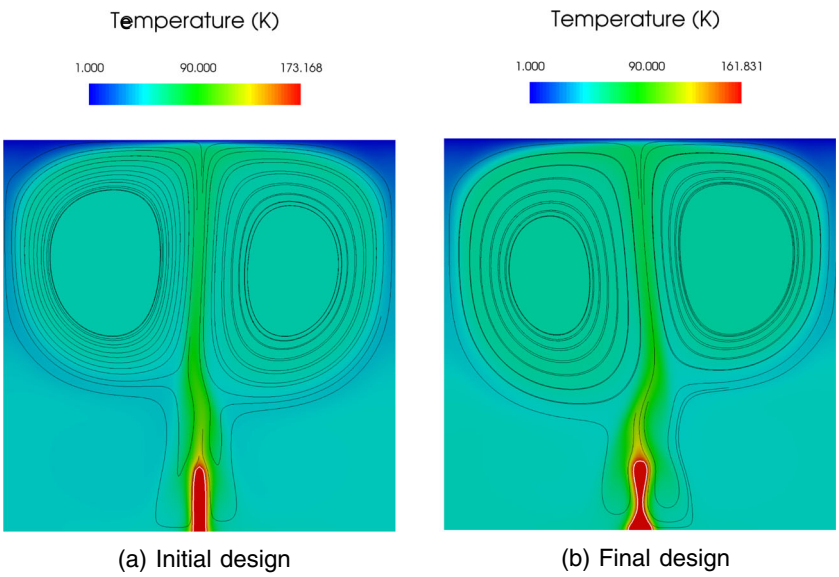

Fig. 13 Snapshot of temperature contours with streamlines for 2D transient topology optimization

Table 8 2D unsteady topology optimization results

Design	Initial design	Final design
$mean(T_B)\ [K]$	1.74×10^2	1.61×10^2
Volume $[m^3]$	3.83×10^{-5}	3.89×10^{-5}
Perimeter $[m^2]$	3.01×10^{-2}	3.46×10^{-2}
Rayleigh	1.60×10^7	1.48×10^7
Grashof	2.70×10^7	2.50×10^7
Local Reynolds	2.70×10^3	2.69×10^3

for specific operating conditions and the resulting flow regimes.

Accounting for the (potentially) transient behavior of natural convection problems in the design approach allows for the consideration of a larger range of Rayleigh and Grashof numbers and increases confidence in the accuracy of the flow and thermal analysis. However, these advantages come at significant additional computational cost. Due to the serial nature of the time stepping schemes used in both the forward and sensitivity analyses, the computational cost per optimization iteration increases linearly with the number of time steps required. Owing to the time scales dominating the flow and thermal responses, a large number of time steps is needed to reach a quasi-steady-state response in the solid phase. In addition, a rather fine mesh is required to resolve spatially the flow. Here the XFEM model yields about 25,000 degrees of freedom; the exact number depends on the intersection configuration. The total time for a forward and sensitivity analysis was approximately 2 hours, using MUMPS for solving the linear sub-problems on a desktop computer with a six-core AMD Phenom II 1090T 3.2GHz processor and 8GB of RAM. For the total of 150 optimization iterations, 12 days' worth of computational time was required. To reduce the computational costs more advanced time integration approaches could be incorporated. Alternative spatial discretization schemes, such as finite volume or discontinuous Galerkin methods, may also increase the computational efficiency.

5.4 3D steady-state topology optimization

Finally, we demonstrate that the proposed optimization framework is also applicable to natural convection problems in three dimensions. Due the significant computational costs of solving transient problems, we limit this study to a low-Grashof number configuration which guarantees steady-state solutions throughout the optimization process.

The natural convection problem of Section 5.2 is extended to three dimensions by rotating the design domain about the center as shown in Fig. 4. The problem parameters are given in Table 9. The radius of the sphere of solid phase around point B is $r_{BS} = 2.5 \times 10^{-3}\ m$. The smoothing radius of the linear filter (15) is $r_f = 1.069 \times 10^{-3}\ m$. We enforce a double-symmetric design by defining the nodal level set functions at corresponding nodes by the same optimization variables. A layer of fluid material, $0.02\ m$ thick, is prescribed at the top surface of the design domain to prevent the design from interacting with the boundary condition applied there.

As in the previous studies we impose constraints on the maximum solid volume and the perimeter. Numerical studies on the 3D configurations showed that small, sub-element-size features may emerge, causing the optimization process to stagnate. To suppress these features, we additionally impose a constraint on the level set gradient measure (16). The constraint limit is set initially to a rather large value which does not prohibit geometric features from merging. As the design converges the constraint values is lowered to remove sub-element-size features. A constraint of $c_g = 1.0 \times 10^{-7}$ is prescribed for 300 optimization iterations, then lowered to $c_g = 1.0 \times 10^{-9}$ for another 300 iterations.

We start the optimization process with a cylindrical solid phase of radius $0.003\ m$ and height $0.005\ m$; a semi-sphere is placed at the top of the cylinder. The flow field of the initial design is characterized by a Rayleigh number of $Ra = 2000$, a Grashof number of $Gr = 3400$, and a maximum local Reynolds number of $Re_{max} = 5.0$. These numbers are similar to the ones of the configuration in Section 5.2 and indicative of a steady-state flow.

The streamlines for the initial and optimized designs are shown in Fig. 15. The performance and flow characteristics are given in Table 10. The geometry of the 3D optimum deviates noticeably from the solution of the 2D steady state problem. While similar to the 2D solution the 3D design

Table 9 3D box topology optimization parameters

Parameter	Value
Domain height	$h = 0.030\ m$
Domain width	$w = 0.030\ m$
Number of elements	51680
Heat flux	$q_B = 3.333 \times 10^{-4}\ W$
Volume constraint	$c_v = 5.24 \times 10^{-7}\ m^3$
Perimeter constraint	$c_{pe} = 4.7 \times 10^{-4}\ m^2$
Gradient constraint	$c_g = [1.0 \times 10^{-7}, 1.0 \times 10^{-9}]\ m$

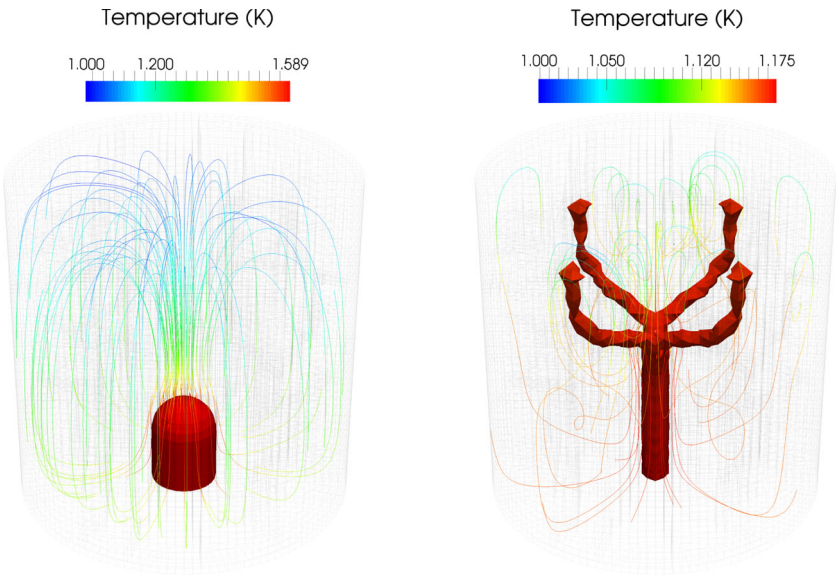

Fig. 15 Results for 3D box design problem

(a) Initial design (b) Final design

consists of a thin base, it splits into four branches in the top half, shown in Fig. 15b. The 3D configuration appears to promote thinner features necessitating some form of feature size control; here implemented via a constraint on the level set gradient measure.

This study demonstrates the applicability of the proposed optimization framework to 3D natural convection problems. However, we point out that the numerical and computationally complexity in solving the forward problem and the overall optimization problem is significantly increased over 2D problems. This includes the numerical stability of the XFEM formulation, in particular the treatment of the interface conditions, as well as the complexity of solving large nonlinear problems. The increased design freedom in 3D allows the emergence of complex geometries for which it is difficult to robustly compute flow solutions using uniformly refined meshes that are not altered in the optimization process.

Table 10 3D topology optimization results

Design	Initial design	Final design
T_B $[K]$	1.59	1.18
Volume $[m^3]$	1.89×10^{-7}	1.46×10^{-7}
Perimeter $[m^2]$	1.47×10^{-4}	3.81×10^{-4}
Rayleigh	2.01×10^{3}	5.99×10^{2}
Grashof	3.41×10^{3}	1.01×10^{3}
Local Reynolds	4.97	2.54×10^{-1}

6 Conclusions

This study presented an explicit LSM for optimizing the geometry of natural convection dominated flows. Our approach expands existing density methods onto transient problems. The energy transport is described by an advection-diffusion model. In the fluid phase, the advective velocity is modeled by the incompressible Navier-Stokes equations and the Boussinesq approximation of the buoyancy forces. In the solid phase, the advective velocity vanishes. The method relies on a XFEM discretization of the governing equations in the fluid and solid phase. The interface conditions are enforced weakly using Nitsche's method. To consider flows exhibiting dynamic instabilities, the flow and temperature fields are advanced in time by an implicit Euler backward time integration scheme. The design sensitivities of the steady-state and transient response are computed by an adjoint approach.

The main characteristics of the proposed method were studied with steady-state problems in 2D and 3D and a 2D transient problem. One of the main advantages of the LSM approach is that it provides a crisp geometry description throughout the optimization process and that it does not suffer from the presence of fictitious material in optimized material distribution, as Alexandersen et al. (2014) reported for density methods. Studies on a 2D steady-state design problem illustrated that non-intuitive asymmetric designs feature improved cooling performance compared to optimized symmetric designs which converged to common fin-type shapes.

A study on a high-Grashof number configuration demonstrated the applicability of the proposed methods to problems where the flow exhibits dynamic instabilities and does not converge to a steady state. However, such problems are stymied by large computational costs as a fine mesh and small time steps are needed to resolve the transient flow and a large number of time steps is required to reach a quasi-steady-state thermal response in the solid. The applicability of the proposed method to 3D problems was illustrated with a low Grashof steady-state problem. For this problem, the need to control the size of geometric features was observed. To this end, a constraint on the gradients of the level set field was imposed, along with setting appropriate lower and upper bounds on the optimization variables. The application of the proposed method to 3D problems is hampered by large computational costs.

The numerical studies have demonstrated the applicability of the proposed method to a broad range of natural convection problems, including three-dimensional problems and problems with unstable, transient flows. Future studies should focus on reducing the computational costs, for example, via adaptive meshing techniques and adaptive time stepping schemes. Furthermore, robust and efficient schemes need to be developed to impose feature size constraints.

Acknowledgments The authors acknowledge the support of the National Science Foundation under grant EFRI-SEED 1038305 and CBET 1246854. The opinions and conclusions presented in this paper are those of the authors and do not necessarily reflect the views of the sponsoring organization.

References

Alexandersen J (2011) Topology optimization for convection problems. Bachelor thesis. DTU Mekanik

Alexandersen J (2015) Topology optimisation of passive coolers for light-emitting diode lamps. In: Proceedings of the 11th World Congress of Structural and Multidisciplinary Optimisation

Alexandersen J, Aage N, Andreasen CS, Sigmund O (2014) Topology optimisation for natural convection problems. Int J Numer Methods Fluids 76(10):699–721

Allaire G, Jouve F, Toader A (2002) A level-set method for shape optimization. Comptes Rendus Mathematique 334(12):1125–1130

Allaire G, Jouve F, Toader AM (2004) Structural optimization using sensitivity analysis and a level-set method. J Comput Phys 194(1):363–393

Amestoy P, Duff I, LExcellent J (1998) MUMPS multifrontal massively parallel solver. Tech. rep., Version 2.0. Technical Report TR/PA/98/02. CERFACS, 42 Ave G. Coriolis, 31057 Toulouse Cedex, France

Bahadur R, Bar-Cohen A (2005) Thermal design and optimization of natural convection polymer pin fin heat sinks. IEEE Trans Compon Packag Technol 28(2):238–246

Baïri A, Zarco-Pernia E, de María JMG (2014) A review on natural convection in enclosures for engineering applications. The particular case of the parallelogrammic diode cavity. Appl Therm Eng 63(1):304–322

Bruns T (2007) Topology optimization of convection-dominated, steady-state heat transfer problems. Int J Heat Mass Transf 50(15–16):2859–2873

Burger M, Osher SJ (2005) A survey in mathematics for industry a survey on level set methods for inverse problems and optimal design. Euro Jnl of Applied Mathematics 16:263–301

Coffin P, Maute K (2015) Level set topology optimization of cooling and heating devices using a simplified convection model. Under review in Structural and Multidisciplinary Optimization

Davis TA (2004) Algorithm 832: Umfpack v4. 3—an unsymmetric-pattern multifrontal method. ACM Trans Math Softw (TOMS) 30(2):196–199

Deaton JD, Grandhi RV (2014) A survey of structural and multidisciplinary continuum topology optimization: post 2000. Struct Multidiscip Optim 49(1):1–38

Dolbow J, Harari I (2009) An efficient finite element method for embedded interface problems. Int J Numer Meth Engng 78:229–252

Franca LP, Frey SL, Hughes TJ (1992) Stabilized finite element methods: I. application to the advective-diffusive model. Comput Methods Appl Mech Eng 95(2):253–276

Fries TP, Belytschko T (2006) The intrinsic XFEM: A method for arbitrary discontinuities without additional unkowns. Int J Numer Methods Eng 68:1358–1385

Fries T, Belytschko T (2010) The extended/generalized finite element method: an overview of the method and its applications. Int J Numer Methods Eng 84(3):253–304

Golmon S, Maute K, Dunn ML (2012) Multiscale design optimization of lithium ion batteries using adjoint sensitivity analysis. Int J Numer Methods Eng 92(5):475–494

Iga A, Nishiwaki S, Izui K, Yoshimura M (2009) Topology optimization for thermal conductors considering design-dependent effects, including heat conduction and convection. Int J Heat Mass Transf 52(11–12):2721–2732

Jenkins N, Maute K (2015) Level set topology optimization of stationary fluid-structure interaction problems. Struct Multidiscip Optim. 1–17. doi:10.1007/s00158-015-1229-9

Khoei AR (2015) Extended finite element method: theory and applications. Wiley

Koga AA, Lopes ECC, Villa Nova HF, Lima CRd, Silva ECN (2013) Development of heat sink device by using topology optimization. Int J Heat Mass Transf 64:759–772

Kontoleontos E, Papoutsis-Kiachagias E, Zymaris A, Papadimitriou D, Giannakoglou K (2013) Adjoint-based constrained topology optimization for viscous flows, including heat transfer. Eng Optim 45(8):941–961

Kreisselmeier G, Steinhauser R (1979) Systematic control design by optimizing a vector performance index. In: International Federation of Active Contrals Symposium on Computer Aided Design of Control Systems, Zurich, Switzerland

Kreissl S, Maute K (2011) Topology optimization for unsteady flow. Int J Numer Methods Eng 87:1229–1253

Kreissl S, Maute K (2012) Levelset based fluid topology optimization using the extended finite element method. Struct Multidiscip Optim 46(3):311–326

Lang C, Makhija D, Doostan A, Maute K (2014) A simple and efficient preconditioning scheme for heaviside enriched XFEM. Comput Mech 54(5):1357–1374

Lee K (2012) Topology optimization of convective cooling system designs. PhD thesis, The University of Michigan

Luo Z, Tong L, Wang MY, Wang S (2007) Shape and topology optimization of compliant mechanisms using a parameterization level set method. J Comput Phys 227(1):680–705

Makhija D, Maute K (2014) Numerical instabilities in level set topology optimization with the extended finite element method. Struct Multidiscip Optim 49(2):185–197

Makhija D, Maute K (2015) Level set topology optimization of scalar transport problems. Struct Multidiscip Optim 51(2):267–285
Marck G, Nemer M, Harion JL (2013) Topology optimization of heat and mass transfer problems: laminar flow. Numerical Heat Transfer, Part B: Fundamentals 63(6):508–539
Matsumori T, Kondoh T, Kawamoto A, Nomura T (2013) Topology optimization for fluid–thermal interaction problems under constant input power. Struct Multidiscip Optim 47(4):571–581
McConnell C, Pingen G (2012) Multi-layer, pseudo 3d thermal topology optimization of heat sinks. In: ASME 2012 International Mechanical Engineering Congress and Exposition, American Society of Mechanical Engineers, pp 2381–2392
Moon H, Kim C, Wang S (2004) Reliability-based topology optimization of thermal systems considering convection heat transfer. In: Proceedings of the 10th AIAA/ISSMO Multidisciplinary Analysis and Optimization Conference, August 30-September 1, Albany, NY
Morrison AT (1992) Optimization of heat sink fin geometries for heat sinks in natural convection. In: InterSociety Conference on Thermal Phenomena in Electronic Systems, 1992. I-THERM III. IEEE, pp 145–148
Nitsche J (1975) Uber ein Variationsprinzip zur Loesung von Dirichlet-Problemen bei Verwendung von Teilraeumen, die keinen Randbedingungen unterworfen sind. Abhandlungen aus dem Mathematischen Seminar der Universitaet Hamburg 36:9–15
Pingen G, Waidmann M, Evgrafov A, Maute K (2010) A parametric level-set approach for topology optimization of flow domains. Struct Multidiscip Optim 41(1):117–131
Schott B, Rasthofer U, Gravemeier V, Wall W (2014) A face-oriented stabilized Nitsche-type extended variational multiscale method for incompressible two-phase flow. Int J Numer Methods Eng. doi:10.1002/nme.4789
Seo JH (2009) Optimal design of material microstructure for convective heat transfer in a solid-fluid mixture. PhD thesis, University of Michigan at Ann Arbor
Sigmund O, Maute K (2013) Topology optimization approaches: a comparative review. Struct Multidiscip Optim 48(6):1031–1055
Svanberg K (2002) A class of globally convergent optimization methods based on conservative convex separable approximations. SIAM J Optim 12(2):555–573
Terada K, Asai M, Yamagishi M (2003) Finite cover method for linear and non-linear analyses of heterogeneous solids. Int J Numer Methods Eng 58(9):1321–1346
Tezduyar TE, Mittal S, Ray SE, Shih R (1992) Incompressible flow computations with stabilized bilinear and linear equal-order-interpolation velocity-pressure elements. Comput Methods Appl Mech Eng 95:221–242
Touihri R, Hadid HB, Henry D (1999) On the onset of convective instabilities in cylindrical cavities heated from below. i. pure thermal case. Phys Fluids (1994-present) 11(8):2078–2088
Tran AB, Yvonnet J, He QC, Toulemonde C, Sanahuja J (2011) A multiple level set approach to prevent numerical artefacts in complex microstructures with nearby inclusions within xfem. Int J Numer Methods Eng 85(11):1436–1459
van Dijk N, Maute K, Langelaar M, Keulen F (2013) Level-set methods for structural topology optimization: a review. Struct Multidiscip Optim 48(3):437–472
Wang MY, Wang X, Guo D (2003) A level set method for structural topology optimization. Comput Methods Appl Mech Eng 192(1–2):227–246
Wang S, Wang M (2006) Radial basis functions and level set method for structural topology optimization. Int J Numer Methods Eng 65(12):2060–2090
Yaji K, Yamada T, Kubo S, Izui K, Nishiwaki S (2015) A topology optimization method for a coupled thermal–fluid problem using level set boundary expressions. Int J Heat Mass Transf 81:878–888
Yamada T, Izui K, Nishiwaki S (2011) A level set-based topology optimization method for maximizing thermal diffusivity in problems including design-dependent effects. J Mech Des 133 (3):031,011
Yin L, Ananthasuresh G (2002) A novel topology design scheme for the multi-physics problems of electro-thermally actuated compliant micromechanisms. Sensors and Actuators A: Physical 97:599–609
Yoon G, Kim Y (2005) The element connectivity parameterization formulation for the topology design optimization of multiphysics systems. Int J Numer Methods Eng 64(12):1649–1677
Yoon GH (2010) Topological design of heat dissipating structure with forced convective heat transfer. J Mech Sci Technol 24:1225–1233